

Strong-coupling superconductivity and weak vortex pinning in Ta-doped CsV₃Sb₅ single crystals

Jinyulin Li¹, Wei Xie¹, Jinjin Liu^{2,3}, Qing Li¹, Xiang Li^{2,3,4}, Huan

Yang^{1,*}, Zhiwei Wang^{2,3,4,†}, Yugui Yao^{2,3}, and Hai-Hu Wen^{1,‡}

¹ National Laboratory of Solid State Microstructures and Department of Physics,

Collaborative Innovation Center of Advanced Microstructures, Nanjing University, Nanjing 210093, China

² Key Laboratory of Advanced Optoelectronic Quantum Architecture and Measurement (MOE),

School of Physics, Beijing Institute of Technology, Beijing 100081, China

³ Beijing Key Lab of Nanophotonics and Ultrafine Optoelectronic Systems,

Beijing Institute of Technology, Beijing 100081, China and

⁴ Material Science Center, Yangtze Delta Region Academy of Beijing Institute of Technology, Jiaxing, 17 314011, China

By measuring magnetizations of pristine and Ta-doped CsV₃Sb₅ single crystals, we have carried out systematic studies on the lower critical field, critical current density, and equilibrium magnetization of this kagome system. The lower critical field has been investigated in the two typical samples, and the temperature dependent lower critical field obtained in Ta-doped sample can be fitted by using the model with two *s*-wave superconducting gaps yielding the larger gap of $2\Delta_{s1}/k_B T_c = 7.9 (\pm 1.8)$. This indicates a strong-coupling feature of the V-based superconductors. The measured magnetization hysteresis loops allow us to calculate the critical current density, which shows a very weak bulk vortex pinning. The magnetization hysteresis loops measured in these two kinds of samples can be well described by a recently proposed generalized phenomenological model, which leads to the determination of many fundamental parameters for these superconductors. Our systematic results and detailed analysis conclude that this V-based kagome system has features of strong-coupling superconductivity, relatively large Ginzburg-Landau parameter and weak vortex coupling.

I. INTRODUCTION

Since the discovery of superconductivity in the kagome compounds AV₃Sb₅ (*A* = K, Rb, or Cs) [1–3], these new materials have raised extensive interests owing to their exotic physics besides superconductivity. Firstly, the charge density wave (CDW) order is observed to coexist with the superconductivity in these materials [1–3]; however, the exact origin of the CDW state is still under debate [4–9]. Secondly, the topological nontrivial state is evidenced to exist in these materials [1, 10, 11]. A robust zero-bias conductance peak is observed in the vortex core on the Cs 2×2 surface of CsV₃Sb₅, and this zero-bias peak is regarded as the possible Majorana zero mode [12]. Thirdly, there are some experiments supporting the argument of symmetry breaking in these materials. Below the CDW transition temperature, an in-plane nematic electronic state is observed in CsV₃Sb₅ by electronic transport measurements [13, 14], which is consistent with the anisotropic intensity of the CDW order in CsV₃Sb₅ and its sister compound from scanning tunnelling microscope (STM) measurements [15–18]. A natural explanation is that the three-dimensional $2 \times 2 \times 2$ or $2 \times 2 \times 4$ CDW order naturally breaks the in-plane symmetry in these materials [12, 19, 20]. Furthermore, the symmetry in the off-plane direction is also complex. A giant anomalous Hall conductivity is observed in this family [21, 22], and a theoretical work of the chiral flux current phase is proposed to explain this effect [5]. Meanwhile, an unconventional chiral charge order is suggested to exist in these materials [16, 23].

Since AV₃Sb₅ is a compound containing the *3d* tran-

sition element of vanadium, the superconductivity in this system is likely to be unconventional. Therefore, the superconducting pairing attracts great interests in these materials. The superconducting gap is argued to be nodal from the thermal conductivity measurement in CsV₃Sb₅ [24]; however, other experimental observations support the existence of the nodeless gap [25, 26]. The STM measurements reveal a superconducting gap Δ of about 0.5 meV in CsV₃Sb₅ [12, 27]. This gap value corresponds to the ratio $2\Delta/k_B T_c$ of about 5 which is larger than the 3.53 expected by the weak-coupling Bardeen-Cooper-Schrieffer (BCS) theory [27]. Meanwhile, the multi-gap feature is observed in CsV₃Sb₅ based on the STM data measured at a much lower temperature, and the absence of in-gap states induced by non-magnetic impurities suggests the sign-preserving gap(s) in this material [28]. The multi-gap superconductivity is also proved by the penetration depth [25, 29] and lower critical field [30] measurements in CsV₃Sb₅.

In order to increase the critical temperature T_c , applying pressure and chemical doping are two effective methods. Up to now, the highest value of T_c can be enhanced to about 4.5 K in the Sn- [31] or the Nb-doped [32] CsV₃Sb₅ single crystals. In materials with coexisting superconducting and CDW phases, the superconductivity is usually enhanced when the CDW is suppressed. However, in CsV₃Sb₅, although the applied pressure or the chemical doping can suppress the CDW state, their influence to T_c is non-monotonic. The second superconducting dome appears near the pressure [33–35] or the Ti- and Sn-doping level [31, 36] where the CDW phase is completely suppressed. This fact suggests the unusual

competition and the complex interplay between superconductivity and CDW in CsV_3Sb_5 .

In this paper, we report comparative studies on the magnetization data measured in the single crystals of CsV_3Sb_5 and $\text{Cs}(\text{V}_{1-x}\text{Ta}_x)_3\text{Sb}_5$ with $x \approx 0.14$. We obtain several superconducting parameters of the pristine and Ta-doped samples, including the lower and upper critical fields, the Ginzburg-Landau parameter, the penetration depth, and the coherence length.

II. EXPERIMENTAL METHOD

The pristine and Ta-doped CsV_3Sb_5 single crystals were grown by the self-flux method [1, 37–39]. Here we choose the $\text{Cs}(\text{V}_{1-x}\text{Ta}_x)_3\text{Sb}_5$ single crystal with the elemental doping level of $x \approx 0.14$, and this is nearly the highest doping level x_{max} we can achieve. Since T_c increases almost monotonously with x when $x \leq x_{\text{max}} = 0.14$ [37], the single crystal with $x = 0.14$ has the highest T_c so far when compared to other samples with a lower doping level. The magnetization measurements were carried out in a SQUID-VSM (Quantum Design) with the lowest temperature of 1.8 K. The frequency of the vibration is 13.1 Hz. The magnet was degaussed before a new round of measurement for the lower critical field (H_{c1}). During the measurements of H_{c1} of undoped and Ta-doped samples and the magnetization hysteresis loops (MHLs) of CsV_3Sb_5 , since the field range is rather narrow, each time of the magnetization measurement was carried out when the target magnetic field was set precisely. During the measurements of MHLs of the Ta-doped sample, the magnetization measurement was carried out while the magnetic field was sweeping. The background signal of the MHL was measured for the sample holder without any samples in the same field varying condition, and the MHLs shown in this work are the results after subtracting the background. The resistivity measurement was carried out by using the standard four-probe method in a PPMS (Quantum Design) with the lowest temperature of 1.9 K. In all measurements, the magnetic field is applied along the c axis of the single crystal.

III. RESULTS

A. Characterization of superconducting transition

Figure 1(a) shows the temperature dependent magnetic susceptibility measured in Ta-doped and undoped CsV_3Sb_5 both in the zero-field-cooled mode under the applied magnetic field of 5 Oe. The magnetic susceptibility of CsV_3Sb_5 shows obvious temperature dependent behavior below the superconducting transition temperature, which may suggest that the magnetic field of 5 Oe is enough to penetrate the sample at the edge at 1.8 K if the

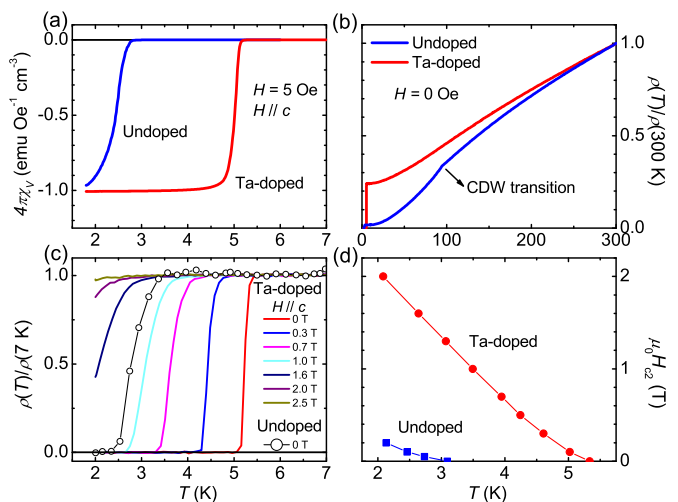


FIG. 1. (a) Temperature dependence of the magnetic susceptibility measured in undoped and Ta-doped single crystals, and the measurements are both carried out in the zero-field-cooled process. Here the demagnetization factor N_{exp} is considered when we calculate the magnetic susceptibility, and N_{exp} is derived from the linear fitting to the initial M - H curve (see main text in Part III B). (b) Temperature dependence of the normalized resistivity measured in the pristine and the Ta-doped samples at temperatures from 2 K to 300 K. (c) Temperature dependent normalized resistivity near the superconducting transition measured in the Ta-doped sample under different magnetic fields and in CsV_3Sb_5 at 0 T. (d) Temperature dependent upper critical field of the pristine and the Ta-doped samples. The upper critical field of CsV_3Sb_5 is taken from the in-plane resistivity data in Ref. [13].

demagnetization factor is considered. However, the magnetic susceptibility of Ta-doped sample shows a plateau with the value about -1 in the low temperature region, indicating a perfect diamagnetism at 1.8 K and under the same field of 5 Oe. The difference of the M - T curves measured in two samples suggests an obvious enhancement of the critical temperature T_c with the Ta doping, and the lower critical field may also be enhanced simultaneously. Figure 1(b) shows the temperature dependent normalized resistivity of the two samples; both curves are normalized by the corresponding resistivity measured at 300 K. One can also see the obvious enhancement of T_c by the Ta doping. Meanwhile, the Ta doping leads to a stronger impurity scattering in the sample and results in a decrease of $RRR \equiv \rho(T = 300 \text{ K})/\rho(T = 6 \text{ K})$ from 59 in the undoped sample to 4.2 in the Ta-doped sample. The kink feature is supposed to be associated with the CDW transition in the temperature dependent resistivity curve measured in CsV_3Sb_5 . However, this feature is disappeared in the resistivity curve measured in doped sample, which suggests a complete suppression of the CDW order by the Ta doping at this doping level. The evolution of the CDW state and the superconductivity by the Ta doping can be seen in Ref. [37]. Figure 1(c) shows the temperature dependence of the normalized resistivity

of the Ta-doped sample measured under different magnetic fields and that of the undoped sample measured at 0 T. By using the criterion of 90% of the normal-state resistivity, the onset transition temperature T_c^{onset} at 0 T is about 3.1 K for the undoped sample and 5.3 K for the Ta-doped sample. T_c^{onset} of CsV_3Sb_5 is similar to values in previous reports by using the same criterion [1, 22, 29], and T_c^{onset} of Ta-doped CsV_3Sb_5 is higher than the highest value of about 4.5 K in the Sn- [31] or the Nb-doped [32] CsV_3Sb_5 single crystals. We can also determine the upper critical field ($\mu_0 H_{c2}$) by using the criterion of 90% of the normal-state resistivity, and Fig. 1(d) shows $\mu_0 H_{c2}(T)$ curve measured in Ta-doped sample. In order to compare the results, we also plot $\mu_0 H_{c2}(T)$ of CsV_3Sb_5 [13] in the same figure. One can see that the Ta doping not only increases T_c but also raises $\mu_0 H_{c2}(T)$ significantly.

B. Lower critical field

In the following, we focus on the magnetic field penetration process in the pristine and the Ta-doped CsV_3Sb_5 single crystals. The sample size used in the following magnetization measurement is $2.4 \times 2.25 \times 0.08 \text{ mm}^3$ for CsV_3Sb_5 , and is $1.18 \times 0.74 \times 0.058 \text{ mm}^3$ for the Ta-doped sample. Figure 2 shows the field dependence of magnetization from the Meissner shielding state to the field penetration state. In this Meissner shielding state, the diamagnetic signal changes almost linearly with the magnetic field in the initial part of the M - H curve, and then the curve deviates from the linear relationship suggesting that the field starts to penetrate into the sample in the form of vortices. It should be noted that both samples are very thin; therefore, the demagnetization factor N should be considered for the analysis of the Meissner shielding effect, and then the relationship between M and H is $-4\pi M = H/(1 - N)$. We linearly fit the initial part of M - H curves and use the fitting results as reference lines describing the perfect diamagnetic state. The fitting lines for the two samples are shown as the dashed lines in Fig. 2, and N_{exp} can be calculated from the formula $-4\pi M = H/(1 - N_{\text{exp}})$. The values of N_{exp} are 0.945 and 0.900 for undoped and Ta-doped samples, respectively. The values of demagnetization factor N_{geo} are 0.910 and 0.858 as calculated from the sizes of the two samples. However, if we use the model of an ellipsoid with three different axes, and the lengths of the three axes are set to be equal to side lengths of the sample, the calculated values of N_{geo} are 0.948 and 0.906 for undoped and Ta-doped samples, respectively. They are very close to values of N_{exp} , which means that the effective shape of a very thin sample may be close to an ellipsoid. However, it should be noted that the magnetization is an output of the SQUID-VSM by fitting to the measured magnetic response of spatially drifting sample (assumed to be a magnetic dipole), which may have an error when compared to the exact value if the sample is

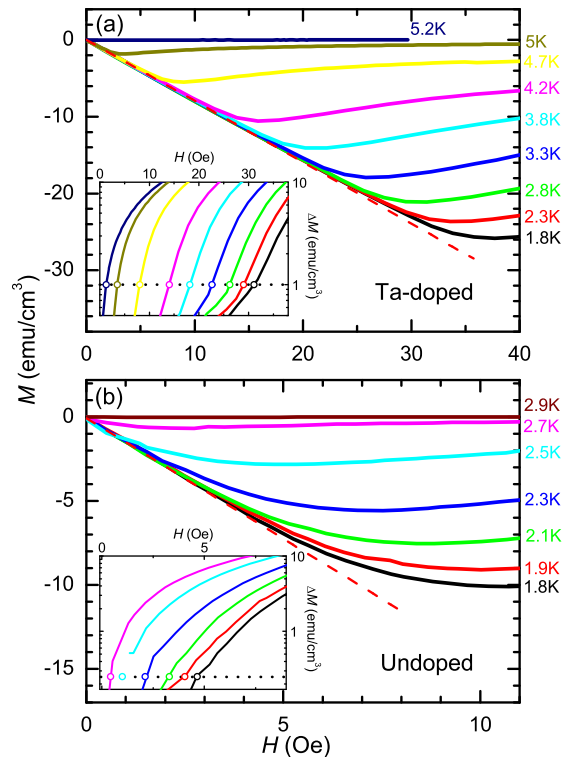


FIG. 2. Magnetic field dependent magnetization measured in (a) Ta-doped CsV_3Sb_5 , and (b) undoped CsV_3Sb_5 at various temperatures. The dashed lines show the linear M - H dependencies representing the perfect diamagnetic property, and the magnetization curves show the field penetration process starting from the perfect diamagnetic state. The insets show the deviation ΔM between the measured magnetization curve and the dashed line in the corresponding main panel. The dotted lines in insets are the criteria to determine H_{c1} , and open circles present the determined values of H_{c1} without considering the demagnetization factor.

very thin. Then, we calculate the differences between the measured M - H curves and two dashed lines, and plot the results in the insets of Fig. 2. The criterion of 1 or 0.25 emu/cm^3 are used to determine the deviation field in the Ta-doped or undoped samples, respectively. And these two criteria are set to be proportional to the maximum values of $-M$ in $-M(H)$ curves at 1.8 K in the two samples. Finally, the exact value of lower critical field H_{c1} can be obtained from the deviation field by multiplying the factor of $1/(1 - N_{\text{exp}})$.

Temperature dependence of the obtained H_{c1} are plotted in Fig. 3 for the Ta-doped and the undoped CsV_3Sb_5 . One can see that H_{c1} is significantly enhanced by the Ta doping. The feature of $H_{c1}(T)$ measured in CsV_3Sb_5 at temperatures down to 0.4 K has been well investigated in a previous work [30]. Therefore, we only analyze the data measured in Ta-doped sample. For a single-band superconductor, H_{c1} or the superfluid density ρ_s can be

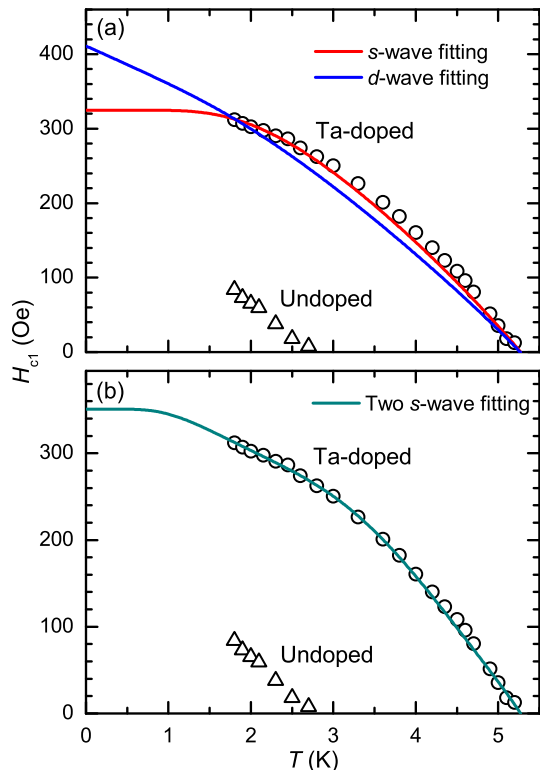


FIG. 3. Temperature dependent experimental data of H_{c1} obtained in the Ta-doped and the undoped CsV_3Sb_5 (symbols). The solid lines are the fitting results to $H_{c1}(T)$ curve obtained in the Ta-doped CsV_3Sb_5 . (a) Fitting results by using a single gap with the gap size of $\Delta_s = 0.8$ meV, and $\Delta_d = 0.98$ meV for a single s - or d -wave gap, respectively. (b) Fitting result by using the model with two s -wave gaps with gap sizes of $\Delta_{s1} = 1.8$ meV, $\Delta_{s2} = 0.43$ meV, and $x_1 = 0.6$ (see text).

expressed as [40, 41],

$$\begin{aligned}
 h_{c1}(T) &\equiv \frac{H_{c1}(T)}{H_{c1}(0)} = \tilde{\rho}_s(T) \equiv \frac{\rho_s(T)}{\rho_s(0)} \\
 &= 1 + 2 \int_0^\infty \frac{df(E, T)}{dE} \frac{E}{\sqrt{E^2 - \Delta(T)^2}} dE. \quad (1)
 \end{aligned}$$

Here, $h_{c1}(T)$ and $\tilde{\rho}_s(T)$ are the normalized lower critical field and superfluid density (ρ_s), $H_{c1}(0)$ and $\rho_s(0)$ are the lower critical field and the superfluid density in zero-temperature limit, $f(E, T)$ is the Fermi function, and $\Delta(T)$ is the superconducting gap function. Figure 3(a) shows the best fitting results by using an s -wave or a d -wave gap. It is obvious that both fitting results can not describe the experimental data well. Since the undoped CsV_3Sb_5 is a multi-gap superconductor, we then fit the data by using the model with two s -wave gaps. The normalized superfluid density in a two-gap system can be expressed as $\tilde{\rho}_s = x_1 \tilde{\rho}_{s,s1} + (1 - x_1) \tilde{\rho}_{s,s2}$ with x_1 the proportion in the total normalized ρ_s from the gap Δ_{s1} ; and the normalized lower critical field can be expressed as

$h_{c1} = x_1 h_{c1,s1} + (1 - x_1) h_{c1,s2}$. One of the best fitting results is shown in Fig. 3(b), and one can see that the fitting curve coincides with the experimental data very well. Here it should be noted that the values of superconducting gaps have some uncertainties because there are several free parameters in the fitting, and the two-gap model can fit the experimental data well with fitting parameters of $\Delta_{s1} = 1.8 \pm 0.4$ meV, $\Delta_{s2} = 0.43 \pm 0.05$ meV. But the two-gap model is required to describe the superconducting gap in the doped sample, anyhow. This conclusion is consistent with that obtained in the undoped CsV_3Sb_5 , in which two s -wave gaps are also required to fit the $H_{c1}(T)$ curve [30]. The two-gap model is also suggested by other kinds of experiments in CsV_3Sb_5 [25, 28, 29]; the obtained larger gap has the value from 0.33 to 0.57 meV, while the smaller gap has the value from 0.13 to 0.36 meV. These gap values obtained in undoped sample are much smaller than those obtained from our data in the Ta-doped sample. Since T_c increases from 3.1 K in the undoped sample to 5.3 K in the Ta-doped sample, the increase of the gap size is expectable.

Here the larger superconducting gap corresponds to a gap ratio of $2\Delta_{s1}/k_B T_c = 7.9 (\pm 1.8)$, while the smaller gap corresponds to $2\Delta_{s2}/k_B T_c = 1.9 (\pm 0.2)$. It should be noted that the expected gap ratio is about 3.53 for a single s -wave superconductor in the weak-coupling limit of the BCS theory, and the value of 3.53 is just between the larger and the smaller gap ratios obtained in Ta-doped CsV_3Sb_5 . Since there are multiple bands ($\text{Sb-}5p_z$ band and $\text{V-}3d$ branch bands) in the CsV_3Sb_5 system, and there are several saddle points near the Fermi energy, the pairing function may consist complex contributions from different scattering channels. In this case, the co-existence of a larger and a smaller gap can be explained in the framework of the BCS theory with two bands if the pairing is established between them [42]. Since it is not clear yet how strong the interband scattering is in the Ta-doped sample, we can probably discuss the situation in different ways with strong and weak interband scattering, respectively. In the case of strong interband scattering, the larger gap can be far above the BCS theoretical value of 3.53 in the weak coupling limit [42], especially here some saddle points with high density of states may be involved in the pair-scattering. Under this particular circumstance, a smaller gap ratio is also anticipated. If the interband scattering is weak, the large gap may be formed by the pair-scattering in some individual bands, here most likely, the strong pairing is due to the intraband pair-scattering of the d -orbitals, and the small gap may be only passively formed. This case resembles that in MgB_2 with a strong pairing gap in σ -band and a weak one in π -band. In any case, the large gap ratio discovered here in Ta-doped CsV_3Sb_5 can be understood as a sign of strong pairing. However, we must emphasize that in a two-gap system with some impurities, like neutron irradiated MgB_2 [43], the interband scattering can exist and play as a fine-tuning factor to adjust the two superconducting gaps and energy-dependent density

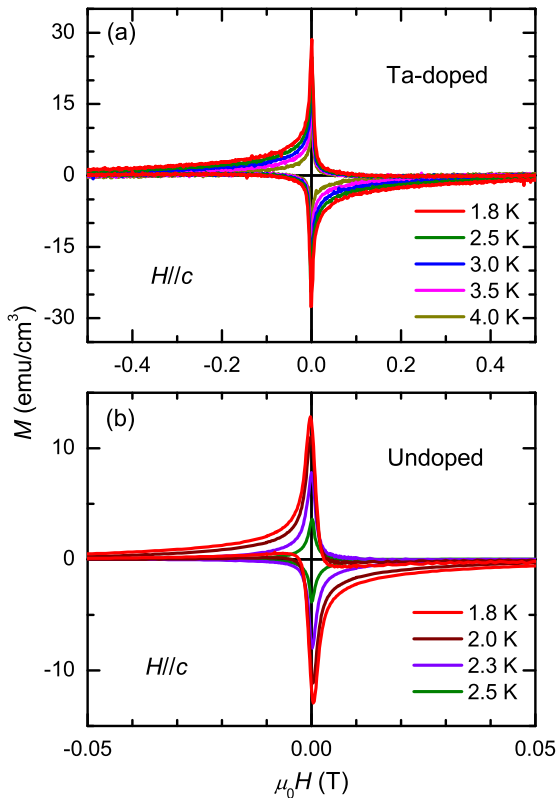


FIG. 4. Magnetization hysteresis loops measured in (a) Ta-doped CsV_3Sb_5 and (b) undoped CsV_3Sb_5 at different temperatures. The field ranges are different in the two figures because the irreversible fields are different for the two samples. MHLs show asymmetry with respect to the axis of $M = 0$ for both samples especially at low temperatures.

of states [44]. In this regard, the momentum-resolved measurements of gap distributions are highly desired for Ta-doped CsV_3Sb_5 .

C. Magnetization hysteresis loop and critical current density

The MHL can provide fruitful information about the critical current density and the vortex pinning properties according to the Bean critical state model. Figure 4 shows MHLs measured in Ta-doped and undoped CsV_3Sb_5 at different temperatures. It should be noted that the irreversible field is low in CsV_3Sb_5 , and especially, the field width at half the maximum is only about 3 mT for the magnetization peak near 0 T at 1.8 K. Therefore, during the measurements of MHLs in CsV_3Sb_5 , the magnetization measurements are carried out when the magnetic field is fixed at the target value. In contrast, because the irreversible field is much larger in the Ta-doped sample, MHLs are measured simultaneously when

the magnetic field sweeps at a rate of 20 Oe/s. Usually, MHLs are symmetric with respect to the axis of $M = 0$ especially at low temperatures in superconductors with a strong bulk vortex pinning. However, one can see in Fig. 4 that the MHLs obtained in both samples reveal obvious asymmetry relative to the axis of $M = 0$. This fact suggests a very weak bulk pinning in both samples. In such case, the magnetization due to the bulk pinning is comparable with the equilibrium magnetization, thus the MHL is very asymmetric. One may argue that the asymmetry of the MHLs were due to the measurements with a slow field sweeping rate, thus the metastable vortex state is quickly relaxed during the measurement. In order to eliminate this concern, we also try a quick sweeping rate of 100 Oe/s for the Ta-doped sample, and the asymmetric shape of the MHL to the axis of $M = 0$ is similar to that shown in Fig. 4(a) although the hysteresis width does increase in high-field region. We argue that the asymmetry of MHLs is an intrinsic feature due to the relatively weak bulk pinning in this family of materials.

It should be noted that a complete MHL consists of the field-ascending and field-descending branches. Here we define M_- or M_+ as the magnetization at some magnetic fields in the field-descending or field-ascending branch of an MHL, and the hysteresis width ΔM can be defined as $\Delta M = M_- - M_+$. Based on the Bean critical state model [45], ΔM is supposed to be proportional to the critical current density J_c . As mentioned above, the vortex state is relaxed in our measurements due to the slow field sweeping rate. Therefore, we use ΔM to calculate the transient current density J_s instead of the intrinsic critical current density J_c [46], and J_s should be lower than J_c . Then, the Bean critical state model [45] is used to calculate J_s , i.e., $J_s = 20\Delta M/[a(1 - a/3b)]$. In the calculation, the unit of ΔM is emu/cm^3 , and a and b are the width and length of the sample with the unit of cm. Figures 5(a) and 5(b) show the field dependence of the calculated J_s in the semilogarithmic plot. As can be seen, the magnitude of J_s is very small in both samples, and the value decreases rapidly with the increase of the field in both samples. All these indicate a very weak bulk vortex pinning in the two samples. Having a close look, one finds that J_s of the Ta-doped and the undoped CsV_3Sb_5 shown in Figs. 5(a) and 5(b) decreases in different slopes with the increase of the applied magnetic field in the high-field region. However, it should be noted that the typical size of the Ta-doped single crystal is much smaller than that of the undoped sample. For instance, the volume of the CsV_3Sb_5 sample used in the magnetization measurement is one order of magnitude larger than that of the Ta-doped sample. Therefore, the discernible magnetization is much larger in the undoped sample. The decrease of J_s in Fig. 5(a) may correspond to the larger J_s part ($J_s > 10^2 \text{ A}/\text{cm}^2$) in Fig. 5(b). Figures 5(c) and 5(d) show the field dependent J_s in the log-log plot. One can see that a power-law relationship of $J_s \propto (\mu_0 H)^{-\mu}$ is satisfied in the low-field region. This power-law decaying behavior suggests the existence of dense pinning centers

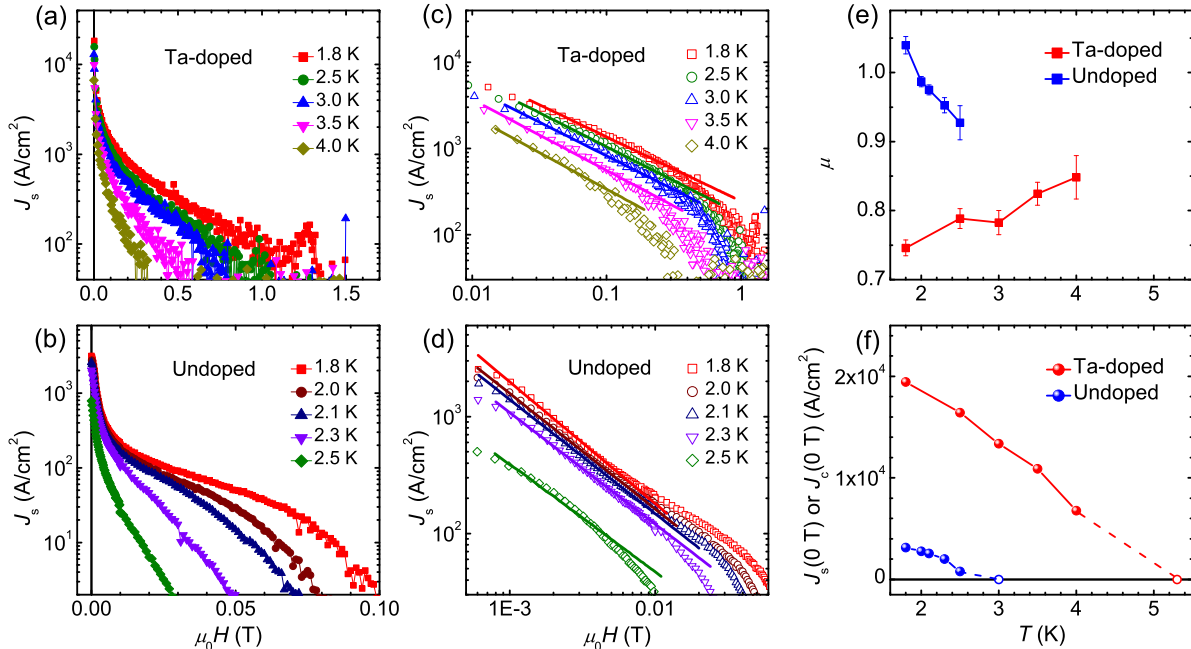


FIG. 5. (a,b) Semilogarithmic plots and (c,d) log-log plots of field dependent J_s measured in Ta-doped and undoped CsV_3Sb_5 . The solid lines in (c,d) are fitting results by using the formula of $J_s \propto (\mu_0 H)^{-\mu}$. (e) Temperature dependent exponent μ derived from fittings in (c,d). (f) Temperature dependence of $J_s(0 \text{ T})$ obtained from (a) and (b), respectively. Empty symbols represent zero-resistance temperatures at 0 T derived from Fig. 1(d), and the corresponding current density $J_c(0 \text{ T})$ is very close to 0 A/cm^2 in resistive measurements.

with very weak pinning strength in the sample, and it can be explained by the collective pinning model as the consequence of the field dependent vortex lattice rigidity [47–49]. Figure 5(e) shows the temperature dependence of the exponent μ obtained from fittings. One can see that μ is in the range of 0.93–1.04 for the undoped sample, and that is 0.75–0.85 for the Ta-doped sample. Since the field interval is much smaller for MHL measurements in the undoped sample than that in the Ta-doped sample, the field range is different when shown in the logarithmic coordinate. That may be the reason for different values and different temperature dependent behaviors of the exponent.

In Fig. 5(f), we plot the temperature dependent J_s at 0 T. It should be noted that the vortex relaxation is relatively weak when the magnetic field is low [50], and then the difference of ΔM at different field sweeping rates is much smaller at 0 T than those at other finite fields (see Ref. [51] for example). Therefore, J_s is closer to J_c at 0 T than at other finite fields. We also plot the zero-resistance temperatures corresponding to the $J_c \approx 0$ in Fig. 5(f), because the current density is extremely low (about several A/cm^2) for resistive measurements. The discontinuous evolution from $J_s(T)$ from magnetization measurements to J_c from resistive measurement may be due to the relaxation of the vortex motion in the measurements of MHLs. At 1.8 K, $J_s(0 \text{ T})$ are 1.94×10^4

A/cm^2 and $3.1 \times 10^3 \text{ A}/\text{cm}^2$ for Ta-doped and undoped CsV_3Sb_5 , respectively. Although $J_s(0 \text{ T})$ is greatly enhanced in the Ta-doped sample, the practical value is still much lower than that of many other unconventional superconductors such as iron-based superconductors [52–54] and cuprates [55] whose critical current densities are normally in a range of 10^5 – $10^7 \text{ A}/\text{cm}^2$ under the same reduced temperature of T/T_c . The relatively low J_s suggests again the very weak pinning in these materials.

D. MHLs fitted by a generalized phenomenological model

Recently, a generalized phenomenological model is developed to describe the magnetic field penetration and MHLs in a type-II superconductor [56], and this model can fit MHLs obtained in Nb and $\text{Ba}_{0.6}\text{K}_{0.4}\text{Fe}_2\text{As}_2$ very well. In the fitting process, the equilibrium and the non-equilibrium magnetization components are considered separately. Here the equilibrium part is the average of the magnetization in the field-ascending and field-descending processes of MHLs, i.e., $M_{\text{equ}} = (M_+ + M_-)/2$; while the non-equilibrium part is the magnetization difference between the field-ascending and field-descending processes, i.e., $M_{\text{pin}} = (M_+ - M_-)/2$. In this model [56], when the width of the sample is much larger than the penetration

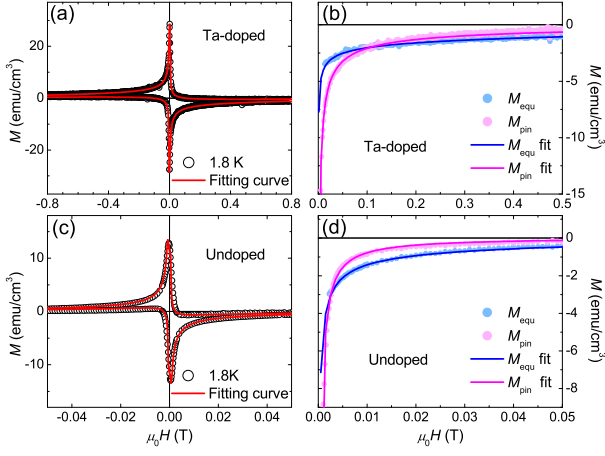


FIG. 6. (a),(c) Magnetization hysteresis loops (open circles) measured in (a) Ta-doped and (c) undoped CsV_3Sb_5 at 1.8 K. (b),(d) Equilibrium and non-equilibrium components of the total magnetization in (b) Ta-doped and (d) undoped CsV_3Sb_5 . The solid curves in the figures show the fitting results by using the phenomenological model [56].

depth λ , M_{equ} is due to the surface screening current within the depth of λ , while the non-equilibrium magnetization M_{pin} comes from the bulk pinning with the depth from λ to the inner. At an external magnetic field $H > H_{c1}$, these two kinds of magnetization with the unit of emu/cm^3 can be expressed as [56]

$$4\pi(1-N)M_{\text{equ}} = -\frac{H_{c1}(H_{c2}-H)}{H_{c2}-H_{c1}} \left(\frac{H_{c1}}{H}\right)^\alpha, \quad (2)$$

$$M_{\text{pin}} = J_c(0 \text{ T}) \frac{b}{20} \frac{H_{c2}-|H_e|}{H_{c2}} \left(\frac{H_{c1}}{H_{c1}+|H_e|}\right)^\beta. \quad (3)$$

Here $H_e = 4\pi(1-N)M_{\text{equ}} + H$ is the field at the depth of λ , and the units of all fields are Oe in equations above. In the fitting, the magnetization is modified by the demagnetization factor N in order to satisfy the boundary condition of field-penetrating process. $J_c(0 \text{ T})$ is the zero-field critical current density and b is the half-width of the sample; the corresponding units of them are A/cm^2 and cm , respectively. α and β are dimensionless fitting parameters which reflect field decaying rates of the magnetization in the equilibrium and non-equilibrium processes. If other parameters are fixed, the MHL will be more asymmetric when α is smaller.

Figures 6(b) and 6(d) show the calculated equilibrium and non-equilibrium components of the MHLs measured at 1.8 K. Usually the non-equilibrium component should be much larger than the equilibrium one [56]; however, one can see that these two components have the similar magnitudes in Ta-doped and undoped CsV_3Sb_5 . This again suggests a very weak bulk pinning in these materials. Since $H_{c2} \gg H_{c1}$ in Ta-doped and undoped

CsV_3Sb_5 , they are obviously type-II superconductors, and then we can try the newly proposed model to fit MHLs obtained in these material. The fitting results are shown in Figs. 6(b) and 6(d) as solid curves, and one can see that they can describe the experimental data very well. With the obtained fitting results of the field dependent M_{equ} and M_{pin} , we can derive MHL in the region $|H| > H_{c1}$. The MHL in the narrow field region of $|H| < H_{c1}$ can be calculated by the integral of field distribution in a specific penetration stage [56]. The general fitting result to the MHLs are shown in Figs. 6(a) and 6(c) as solid curves, and they are consistent with the experimental data. The fitting parameters are $H_{c1} = 10 \text{ Oe}$ (N not considered), $\mu_0 H_{c2} = 2.3 \text{ T}$, $J_c(0 \text{ T}) = 2 \times 10^4 \text{ A}/\text{cm}^2$, $\alpha = 0.28$, and $\beta = 0.61$ for Ta-doped CsV_3Sb_5 ; and $H_{c1} = 5 \text{ Oe}$ (N not considered), $\mu_0 H_{c2} = 0.18 \text{ T}$, $J_c(0 \text{ T}) = 3 \times 10^3 \text{ A}/\text{cm}^2$, $\alpha = 0.52$, and $\beta = 1.0$ for undoped CsV_3Sb_5 . The values of critical fields are similar to those obtained from the other measurements mentioned above, which verifies the validity of our model.

E. Determination of superconducting parameters

The determination of fundamental parameters such as critical fields and the Ginzburg-Landau parameter are very important for new superconductors. We obtained the values of H_{c1} and H_{c2} from the magnetic penetration and resistive measurements in Parts III A and III B, thus the Ginzburg-Landau parameter κ can be calculated from the formula of $H_{c1}/H_{c2} = \ln \kappa / 2\kappa^2$ according to the Ginzburg-Landau theory. In addition, the penetration depth λ_{ab} and the coherence length ξ_{ab} can be deduced, i.e., $H_{c1} = \Phi_0 \ln \kappa / 4\pi\lambda^2$ for λ , and $H_{c2} = \Phi_0 / 2\pi\xi^2$ for ξ . Here Φ_0 is the magnetic flux quantum. We can also calculate the depairing current density based on the formula of $J_d = \Phi_0 / 3\sqrt{3}\pi\mu_0\xi\lambda^2$. Table I lists the superconducting parameters obtained in this work, and all parameters are the values at the temperature of 1.8 K. Here values of $\mu_0 H_{c2}$ at 1.8 K are obtained from linear extrapolations of $\mu_0 H_{c2}(T)$ curves in Fig. 1(d). And other correlated parameters are derived from these values. The value of the penetration depth determined here in CsV_3Sb_5 is consistent with that obtained from the measurement using a technique based on tunneling diode oscillator [25]. These fundamental superconducting parameters help us to have an in-depth understanding on superconductivity in V-based superconductors. The large value of κ confirms that the Ta-doped and undoped CsV_3Sb_5 samples are typical type-II superconductors. With Ta doping, the critical current density and critical fields increase simultaneously with an increase of T_c . Meanwhile, the penetration depth and the coherence length decrease with the Ta doping. The possible reason may be the completely suppression of the CDW phase, and the superconductivity is enhanced.

TABLE I. Superconducting parameters of Ta-doped and undoped CsV₃Sb₅ at 1.8 K.

	$J_d^{\parallel c}(0 \text{ T})$ (A/cm ²)	$J_s^{\parallel c}(0 \text{ T})$ (A/cm ²)	$H_{c1}^{\parallel c}$ (Oe)	$\mu_0 H_{c2}^{\parallel c}$ (T)	κ	λ_{ab} (nm)	ξ_{ab} (nm)
Cs(V _{0.86} Ta _{0.14}) ₃ Sb ₅ ($T_c = 5.3$ K)	7.2×10^7	1.9×10^4	312	2.2	8.7	106.8	12.2
CsV ₃ Sb ₅ ($T_c = 3.1$ K)	9.1×10^6	3.1×10^3	84	0.3	5.5	182.7	33.1

IV. DISCUSSION

Through the fittings to the $H_{c1}(T)$ data of the two systems, we find that the superconducting gap is strongly enhanced by Ta doping. From the resistivity and magnetization data, we find that the CDW transition in the doped sample is completely suppressed. This clearly indicates a competition between superconductivity and the CDW order. The ratio of $2\Delta_{s1}/k_B T_c = 7.9 (\pm 1.8)$ for the Ta-doped sample puts the system to the class of strong-coupling superconductors.

From the magnetization measurements, we find that the critical current density is very low in Ta-doped and undoped CsV₃Sb₅, i.e., in the order of 10^3 to 10^4 A/cm² at 1.8 K under the self-field. There are two possible reasons for the weak pinning effect: a relatively low superfluid density, or a low density of impurities which act as the pinning centers. However, we argue that a very low superfluid density is unlikely in this family of materials. Based on the London expression for the superfluid density $n_s = m^*/\mu_0 \lambda^2 e^2$, we can obtain the value in use of λ , here m^* is the effective electron mass, μ_0 is the permeability of vacuum, and e is the electric charge. The estimated $n_s \approx 1.1 \times 10^{21}$ cm⁻³ for CsV₃Sb₅ if we take the effective mass $m^* \approx 1.3m_0$ from theoretical calculation [57]. The value of the superfluid density is smaller than the charge carrier density of 1.6×10^{22} cm⁻³ obtained from other experiments [35]; however, such value is not small enough to support a diluted superfluid density in this family of materials. Therefore, it seems probable that the very low critical current density is due to the very weak bulk vortex pinning. Based on the collective pinning theory [58], the critical current density J_c has a relation with J_d as $J_c \sim J_d (f_{\text{pin}}^2 n_i / \epsilon_0^2)^{2/3}$, where f_{pin} is the individual pinning force, n_i is the impurity density, and ϵ_0 is the energy scale of the vortex interaction. Here values of J_d are about 7×10^7 and 9×10^6 A/cm² at 1.8 K for Ta-doped and undoped CsV₃Sb₅, respectively. These values are comparable to 6×10^7 A/cm² in bulk MgB₂ sample [59, 60] or 4×10^7 A/cm² in Ba_{0.6}K_{0.4}Fe₂As₂ [61, 62] at the similar temperature. As a result, the major reason for the low critical current density is due to the very small value of $(f_{\text{pin}}^2 n_i / \epsilon_0^2)^{2/3}$, perhaps mainly because of the small value of impurity density n_i . This is evidenced by the well-arranged triangular vortex lattice observed in STM measurements [28]. By comparison, such triangular vortex lattice has also been observed in 2H-NbSe₂ [63], while J_c is only about 2×10^3 A/cm² obtained in the pure single crystal at 2 K [64].

As mentioned above in Part III C, in superconductors with strong bulk pinning, MHLs are usually sym-

metric to the axis of $M = 0$. However, the MHLs obtained in the Ta-doped and undoped CsV₃Sb₅ are very asymmetric. The symmetric magnetization component to $M = 0$ in MHLs or the non-equilibrium component M_{pin} is positively associated with the bulk vortex pinning strength. In our analysis, the comparable amplitudes of the non-equilibrium and equilibrium components suggest the weak bulk pinning in this family of materials. However, it should be noted that the MHLs become more symmetric at higher temperatures in both samples based on the data shown in Fig. 4. This is very different from the situation in Ba_{0.6}K_{0.4}Fe₂As₂, that MHLs become more asymmetric at higher temperature [56]. With the increase of temperature, the bulk pinning and the surface barrier are both weakened. However, in this family of V-based superconductors, the weakening effect to the bulk pinning due to the temperature increase seems to be smaller than that to the surface barrier, and the extremely weak bulk pinning may cause a temperature insensitive behavior of the bulk pinning effect in these materials. It is expected that the bulk pinning will be enhanced if more impurities or defects are induced in the samples.

V. CONCLUSION

In conclusion, we have carried out extensive studies on magnetizations of the high-quality single crystals of Cs(V_{0.86}Ta_{0.14})₃Sb₅ and CsV₃Sb₅. Being similar to CsV₃Sb₅, the Ta-doped sample is also a multiband superconductor with the larger gap ratio of $2\Delta_{s1}/k_B T_c = 7.9 (\pm 1.8)$ and the smaller gap ratio of $2\Delta_{s2}/k_B T_c = 1.9 (\pm 0.2)$ according to the fitting to the temperature dependent lower critical field. This indicates a strong coupling feature of the superconductivity. Some important superconducting parameters are obtained for this family of materials. It is found that the critical current density is extremely low in these materials because of the very weak bulk vortex pinning. Our results provide fruitful information of superconductivity and vortex pinning in the Ta-doped and undoped CsV₃Sb₅.

ACKNOWLEDGMENTS

This work was supported by National Natural Science Foundation of China (Grants No. 12061131001, No. 11927809, No. 92065109, No. 11734003, No. 11904294 and No. 11904020), National Key R&D Program of China (Grants No. 2022YFA1403201

and 2020YFA0308800), Strategic Priority Research Program (B) of Chinese Academy of Sciences (Grant No. XDB25000000), Beijing Natural Science Foundation (Grants No. Z210006 and Z190006). Z.W. thanks the Analysis & Testing Center at BIT for assistance in facil-

ity support.

* huanyang@nju.edu.cn

† zhiweiwang@bit.edu.cn

‡ hhwen@nju.edu.cn

-
- [1] B. R. Ortiz, S. M. L. Teicher, Y. Hu, J. L. Zuo, P. M. Sarte, E. C. Schueller, A. M. M. Abeykoon, M. J. Krogstad, S. Rosenkranz, R. Osborn, R. Seshadri, L. Balents, J. He and S. D. Wilson, CsV₃Sb₅: A Z₂ topological kagome metal with a superconducting ground state, *Phys. Rev. Lett.* **125**, 247002 (2020).
- [2] B. R. Ortiz, P. M. Sarte, E. M. Kenney, M. J. Graf, S. M. L. Teicher, R. Seshadri and S. D. Wilson, Superconductivity in the Z₂ kagome metal KV₃Sb₅, *Phys. Rev. Mater.* **5**, 034801 (2021).
- [3] Q. Yin, Z. Tu, C. Gong, Y. Fu, S. Yan and H. Lei, Superconductivity and normal-state properties of kagome metal RbV₃Sb₅ single crystals, *Chin. Phys. Lett.* **38**, 037403 (2021).
- [4] H. Tan, Y. Liu, Z. Wang, and B. Yan, Charge density waves and electronic properties of superconducting kagome metals, *Phys. Rev. Lett.* **127**, 046401 (2021).
- [5] X. Feng, K. Jiang, Z. Wang and J. Hu, Chiral flux phase in the Kagome superconductor AV₃Sb₅, *Sci. Bull.* **66**, 1384 (2021).
- [6] M. H. Christensen, T. Birol, B. M. Anderson, and R. M. Fernandes, Theory of the charge density wave in AV₃Sb₅ kagome metals, *Phys. Rev. B* **104**, 214513 (2021).
- [7] Z. Wang, S. Ma, Y. Zhang, H. Yang, Z. Zhao, Y. Ou, Y. Zhu, S. Ni, Z. Lu, H. Chen, K. Jiang, L. Yu, Y. Zhang, X. Dong, J. Hu, H.-J. Gao, and Z. Zhao, Distinctive momentum dependent charge-density-wave gap observed in CsV₃Sb₅ superconductor with topological Kagome lattice, arXiv:2104.05556.
- [8] S. Cho, H. Ma, W. Xia, Y. Yang, Z. Liu, Z. Huang, Z. Jiang, X. Lu, J. Liu, Z. Liu, J. Li, J. Wang, Y. Liu, J. Jia, Y. Guo, J. Liu, and D. Shen, Emergence of new van Hove singularities in the charge density wave state of a topological kagome metal RbV₃Sb₅, *Phys. Rev. Lett.* **127**, 236401 (2021).
- [9] H. Luo, Q. Gao, H. Liu, Y. Gu, D. Wu, C. Yi, J. Jia, S. Wu, X. Luo, Y. Xu, L. Zhao, Q. Wang, H. Mao, G. Liu, Z. Zhu, Y. Shi, K. Jiang, J. Hu, Z. Xu, and X. J. Zhou, Electronic nature of charge density wave and electron-phonon coupling in kagome superconductor KV₃Sb₅, *Nat. Commun.* **13**, 273 (2022).
- [10] Y. Fu, N. Zhao, Z. Chen, Q. Yin, Z. Tu, C. Gong, C. Xi, X. Zhu, Y. Sun, K. Liu, and H. Lei, Quantum transport evidence of topological band structures of kagome superconductor CsV₃Sb₅, *Phys. Rev. Lett.* **127**, 207002 (2021).
- [11] K. Nakayama, Y. Li, T. Kato, M. Liu, Z. Wang, T. Takahashi, Y. Yao, and T. Sato, Multiple energy scales and anisotropic energy gap in the charge-density-wave phase of the kagome superconductor CsV₃Sb₅, *Phys. Rev. B* **104**, L161112 (2021).
- [12] Z. Liang, X. Hou, F. Zhang, W. Ma, P. Wu, Z. Zhang, F. Yu, J.-J. Ying, K. Jiang, L. Shan, Z. Wang, and X.-H. Chen, Three-dimensional charge density wave and surface-dependent vortex-core states in a kagome superconductor CsV₃Sb₅, *Phys. Rev. X* **11**, 031026 (2021).
- [13] Y. Xiang, Q. Li, Y. Li, W. Xie, H. Yang, Z. Wang, Y. Yao, and H. H. Wen, Twofold symmetry of c-axis resistivity in topological kagome superconductor CsV₃Sb₅ with in-plane rotating magnetic field, *Nat. Commun.* **12**, 6727 (2021).
- [14] L. Nie, K. Sun, W. Ma, D. Song, L. Zheng, Z. Liang, P. Wu, F. Yu, J. Li, M. Shan, D. Zhao, S. Li, B. Kang, Z. Wu, Y. Zhou, K. Liu, Z. Xiang, J. Ying, Z. Wang, T. Wu, and X. Chen, Charge-density-wave-driven electronic nematicity in a kagome superconductor, *Nature* **604**, 59 (2022).
- [15] H. Li, H. Zhao, B. R. Ortiz, T. Park, M. Ye, L. Balents, Z. Wang, S. D. Wilson, and I. Zeljkovic, Rotation symmetry breaking in the normal state of a kagome superconductor KV₃Sb₅, *Nat. Phys.* **18**, 265 (2022).
- [16] Y.-X. Jiang, J.-X. Yin, M. M. Denner, N. Shumiya, B. R. Ortiz, G. Xu, Z. Guguchia, J. He, M. S. Hossain, X. Liu, J. Ruff, L. Kautzsch, S. S. Zhang, G. Chang, I. Belopolski, Q. Zhang, T. A. Cochran, D. Multer, M. Litskevich, Z.-J. Cheng, X. P. Yang, Z. Wang, R. Thomale, T. Neupert, S. D. Wilson, and M. Z. Hasan, Unconventional chiral charge order in kagome superconductor KV₃Sb₅, *Nat. Mater.* **20**, 1353 (2021).
- [17] H. Zhao, H. Li, B. R. Ortiz, S. M. L. Teicher, T. Park, M. Ye, Z. Wang, L. Balents, S. D. Wilson, and I. Zeljkovic, Cascade of correlated electron states in a kagome superconductor CsV₃Sb₅, *Nature* **599**, 216 (2021).
- [18] H. Li, S. Wan, H. Li, Q. Li, Q. Gu, H. Yang, Y. li, Z. Wang, Y. Yao, and H.-H. Wen, No observation of chiral flux current in the topological kagome metal CsV₃Sb₅, *Phys. Rev. B* **105**, 045102 (2022).
- [19] H. Li, T. Zhang, T. Yilmaz, Y. Y. Pai, C. E. Marvinney, A. Said, Q. W. Yin, C. S. Gong, Z. J. Tu, E. Vescovo, C. S. Nelson, R. G. Moore, S. Murakami, H. C. Lei, H. N. Lee, B. J. Lawrie, and H. Miao, Observation of unconventional charge density wave without acoustic phonon anomaly in kagome superconductors AV₃Sb₅ (A=Rb, Cs), *Phys. Rev. X* **11**, 031050 (2021).
- [20] B. R. Ortiz, S. M. L. Teicher, L. Kautzsch, P. M. Sarte, N. Ratcliff, J. Harter, J. P. C. Ruff, R. Seshadri, and S. D. Wilson, Fermi surface mapping and the nature of charge-density-wave order in the kagome superconductor CsV₃Sb₅, *Phys. Rev. X* **11**, 041030 (2021).
- [21] S. Y. Yang, Y. Wang, B. R. Ortiz, D. Liu, J. Gayles, E. Derunova, R. G.-Hernandez, L. Šmejkal, Y. Chen, S. S. P. Parkin, S. D. Wilson, E. S. Toberer, T. McQueen, and M. N. Ali, Giant, unconventional anomalous Hall effect in the metallic frustrated magnet candidate, KV₃Sb₅, *Sci. Adv.* **6**, eabb6003 (2020).
- [22] F. H. Yu, T. Wu, Z. Y. Wang, B. Lei, W. Z. Zhuo, J. J. Ying, and X. H. Chen, Concurrence of anomalous Hall effect and charge density wave in a superconducting topo-

- logical kagome metal, *Phys. Rev. B* **104**, L041103 (2021).
- [23] C. Guo, C. Putzke, S. Konyzheva, X. Huang, M. G.-Amigo, I. Errea, D. Chen, M. G. Vergniory, C. Felser, M. H. Fischer, T. Neupert, and P. J. W. Moll, Switchable chiral transport in charge-ordered kagome metal CsV_3Sb_5 , *Nature* (2022). <https://doi.org/10.1038/s41586-022-05127-9>
- [24] C. C. Zhao, L. S. Wang, W. Xia, Q. W. Yin, J. M. Ni, Y. Y. Huang, C. P. Tu, Z. C. Tao, Z. J. Tu, C. S. Gong, H. C. Lei, Y. F. Guo, X. F. Yang, and S. Y. Li, Nodal superconductivity and superconducting domes in the topological kagome metal CsV_3Sb_5 , arXiv:2102.08356.
- [25] W. Duan, Z. Nie, S. Luo, F. Yu, B. R. Ortiz, L. Yin, H. Su, F. Du, A. Wang, Y. Chen, X. Lu, J. Ying, S. D. Wilson, X. Chen, Y. Song, and H. Yuan, Nodeless superconductivity in the kagome metal CsV_3Sb_5 , *Sci. China-phys. Mech. Astron.* **64**, 107462 (2021).
- [26] C. Mu, Q. Yin, Z. Tu, C. Gong, H. Lei, Z. Li, and J. Luo, S-wave superconductivity in kagome metal CsV_3Sb_5 revealed by $^{121/123}\text{Sb}$ NQR and ^{51}V NMR measurements, *Chin. Phys. Lett.* **38**, 077402 (2021).
- [27] H. Chen, H. Yang, B. Hu, Z. Zhao, J. Yuan, Y. Xing, G. Qian, Z. Huang, G. Li, Y. Ye, S. Ma, S. Ni, H. Zhang, Q. Yin, C. Gong, Z. Tu, H. Lei, H. Tan, S. Zhou, C. Shen, X. Dong, B. Yan, Z. Wang, and H.-J. Gao, Roton pair density wave in a strong-coupling kagome superconductor, *Nature* **599**, 222 (2021).
- [28] H.-S. Xu, Y.-J. Yan, R. Yin, W. Xia, S. Fang, Z. Chen, Y. Li, W. Yang, Y. Guo, and D.-L. Feng, Multiband superconductivity with sign-preserving order parameter in kagome superconductor CsV_3Sb_5 , *Phys. Rev. Lett.* **127**, 187004 (2021).
- [29] R. Gupta, D. Das, C. H. Mielke III, Z. Guguchia, T. Shiroka, C. Baines, M. Bartkowiak, H. Luetkens, R. Khasanov, Q. Yin, Z. Tu, C. Gong, and H. Lei, Microscopic evidence for anisotropic multigap superconductivity in the CsV_3Sb_5 kagome superconductor, *npj Quantum Mater.* **7**, 49 (2022).
- [30] S. Ni, S. Ma, Y. Zhang, J. Yuan, H. Yang, Z. Lu, N. Wang, J. Sun, Z. Zhao, D. Li, S. Liu, H. Zhang, H. Chen, K. Jin, J. Cheng, L. Yu, F. Zhou, X. Dong, J. Hu, H.-J. Gao, and Z. Zhao, Anisotropic superconducting properties of kagome metal CsV_3Sb_5 , *Chin. Phys. Lett.* **38**, 057403 (2021).
- [31] Y. M. Oey, B. R. Ortiz, F. Kaboudvand, J. Frassinetti, E. Garcia, R. Cong, S. Sanna, V. F. Mitrović, R. Seshadri, and S. D. Wilson, Fermi level tuning and double-dome superconductivity in the kagome metal $\text{CsV}_3\text{Sb}_{5-x}\text{Sn}_x$, *Phys. Rev. Mater.* **6**, L041801 (2022).
- [32] Y. Li, Q. Li, X. Fan, J. Liu, Q. Feng, M. Liu, C. Wang, J.-X. Yin, J. Duan, X. Li, Z. Wang, H.-H. Wen, and Y. Yao, Tuning the competition between superconductivity and charge order in kagome superconductor $\text{Cs}(\text{V}_{1-x}\text{Nb}_x)_3\text{Sb}_5$, *Phys. Rev. B* **105**, L180507 (2022).
- [33] K. Y. Chen, N. N. Wang, Q. W. Yin, Y. H. Gu, K. Jiang, Z. J. Tu, C. S. Gong, Y. Uwatoko, J. P. Sun, H. C. Lei, J. P. Hu, and J.-G. Cheng, Double superconducting dome and triple enhancement of T_c in the kagome superconductor CsV_3Sb_5 under high pressure, *Phys. Rev. Lett.* **126**, 247001 (2021).
- [34] Q. Wang, P. Kong, W. Shi, C. Pei, C. Wen, L. Gao, Y. Zhao, Q. Yin, Y. Wu, G. Li, H. Lei, J. Li, Y. Chen, S. Yan, and Y. Qi, Charge density wave orders and enhanced superconductivity under pressure in the kagome metal CsV_3Sb_5 , *Adv. Mater. (Weinheim)* **33**, 2102813 (2021).
- [35] X. Chen, X. Zhan, X. Wang, J. Deng, X.-B. Liu, X. Chen, J.-G. Guo, and X. Chen, Highly robust reentrant superconductivity in CsV_3Sb_5 under pressure, *Chin. Phys. Lett.* **38**, 057402 (2021).
- [36] H. Yang, Z. Huang, Y. Zhang, Z. Huang, Z. Zhao, J. Shi, H. Luo, L. Zhao, G. Qian, H. Tan, B. Hu, K. Zhu, Z. Lu, H. Zhang, J. Sun, J. Cheng, C. Shen, X. Lin, B. Yan, X. Zhou, Z. Wang, S. J. Pennycook, H. Chen, X. Dong, W. Zhou, and H.-J. Gao, Titanium doped kagome superconductor $\text{CsV}_{3-x}\text{Ti}_x\text{Sb}_5$ and two distinct phases, arXiv:2110.11228.
- [37] K. Okazaki, Y. Zhong, J. Liu, X. Wu, M. Akifumi, Y. Li, S. Najafzadeh, X. Han, T. Kondo, J. Hu, S. Shin, J.-X. Yin, Z. Wang, X. Shi, and Y. Yao, Nodeless electron pairing in CsV_3Sb_5 -derived kagome superconductors, 2022, PREPRINT (Version 1) available at Research Square [<https://doi.org/10.21203/rs.3.rs-1876119/v1>].
- [38] B. R. Ortiz, L. C. Gomes, J. R. Morey, M. Winiarski, M. Bordelon, J. S. Mangum, I. W. H. Oswald, J. A. R.-Rivera, J. R. Neilson, S. D. Wilson, E. Ertekin, T. M. McQueen, and E. S. Toberer, New kagome prototype materials: discovery of KV_3Sb_5 , RbV_3Sb_5 , and CsV_3Sb_5 , *Phys. Rev. Mater.* **3**, 094407 (2019).
- [39] Z. Wang, Y.-X. Jiang, J.-X. Yin, Y. Li, G.-Y. Wang, H.-L. Huang, S. Shao, J. Liu, P. Zhu, N. Shumiya, M. S. Hossain, H. Liu, Y. Shi, J. Duan, X. Li, G. Chang, P. Dai, Z. Ye, G. Xu, Y. Wang, H. Zheng, J. Jia, M. Z. Hasan, and Y. Yao, Electronic nature of chiral charge order in the kagome superconductor CsV_3Sb_5 , *Phys. Rev. B* **104**, 075148 (2021).
- [40] A. Carrington and F. Manzano, Magnetic penetration depth of MgB_2 , *Physica C* **385**, 205 (2003).
- [41] H. G. Luo and T. Xiang, Superfluid response in electron-doped cuprate superconductors, *Phys. Rev. Lett.* **94**, 027001 (2005).
- [42] H. Suhl, B. T. Matthias, and L. R. Walker, Bardeen-Cooper-Schrieffer theory of superconductivity in the case of overlapping bands, *Phys. Rev. Lett.* **3**, 552 (1959).
- [43] M. Putti, P. Brotto, M. Monni, E. G. D'Agliano, A. Sanna, and S. Massidda, Intraband vs. interband scattering rate effects in neutron irradiated MgB_2 , *EPL* **77**, 57005 (2007).
- [44] Y. Ohashi, Effects of interband impurity scattering on superconducting density of states in a two-band superconductor, *Physica C* **412-414**, 41 (2004).
- [45] C. P. Bean, Magnetization of high-field superconductors, *Rev. Mod. Phys.* **36**, 31 (1964).
- [46] H. G. Schnack, R. Griessen, J. G. Lensink, and H.-H. Wen, Generalized inversion scheme for the determination of activation energies from flux-creep experiments in high- T_c superconductors, *Phys. Rev. B* **48**, 13178 (1993).
- [47] A. I. Larkin and Y. N. Ovchinnikov, Pinning in type II superconductors, *J. Low Temp. Phys.* **34**, 409 (1979).
- [48] A. Duarte, E. Fernandez Righi, C. A. Bolle, F. de la Cruz, P. L. Gammel, C. S. Oglesby, E. Bucher, B. Batlogg, and D. J. Bishop, Dynamically induced disorder in the vortex lattice of $2H\text{-NbSe}_2$, *Phys. Rev. B* **53**, 11336 (1996).
- [49] M. T. Li, Y. F. Fang, Z. Sun, J. C. Zhang, and C. T. Lin, Evidence for weak collective pinning and δl pinning in topological superconductor $\text{Cu}_x\text{Bi}_2\text{Se}_3$, *J. Phys.: Condens. Matter* **30**, 31LT01 (2018).
- [50] H. H. Wen, A. F. Th. Hoekstra, R. Griessen, S. L. Yan,

- L. Fang, and M. S. Si, Field induced vanishing of the vortex glass temperature in $Tl_2Ba_2CaCu_2O_8$ thin films, *Phys. Rev. Lett.* **79**, 1559 (1997).
- [51] H. Yang, C. Ren, L. Shan, and H.-H. Wen, Magnetization relaxation and collective vortex pinning in the Fe-based superconductor $SmFeAsO_{0.9}F_{0.1}$, *Phys. Rev. B* **78**, 092504 (2008).
- [52] H. Yang, H. Luo, Z. Wang, and H.-H. Wen, Fishtail effect and the vortex phase diagram of single crystal $Ba_{0.6}K_{0.4}Fe_2As_2$, *Appl. Phys. Lett.* **93**, 142506 (2008).
- [53] L. Fang, Y. Jia, V. Mishra, C. Chaparro, V. K. V.-Vlasov, A. E. Koshelev, U. Welp, G. W. Crabtree, S. Zhu, N. D. Zhigadlo, J. Karpinski, and W. K. Kwok, Huge critical current density and tailored superconducting anisotropy in $SmFeAsO_{0.85}F_{0.15}$ by low-density columnar-defect incorporation, *Nat. Commun.* **4**, 2655 (2013).
- [54] S. J. Singh, M. Bristow, W. R. Meier, P. Taylor, S. J. Blundell, P. C. Canfield, and A. I. Coldea, Ultrahigh critical current densities, the vortex phase diagram, and the effect of granularity of the stoichiometric high- T_c superconductor $CaKFe_4As_4$, *Phys. Rev. Mater.* **2**, 074802 (2018).
- [55] C. He, X. Ming, J. Si, X. Zhu, J. Wang, and H.-H. Wen, Characterization of the $(Cu,C)Ba_2Ca_3Cu_4O_{11+\delta}$ single crystals grown under high pressure, *Supercond. Sci. Technol.* **35**, 025004 (2022).
- [56] W. Xie, Y.-H. Liu, and H.-H. Wen, Generalized phenomenological model for the magnetic field penetration and magnetization hysteresis loops of a type-II superconductor, *Phys. Rev. B* **105**, 014505 (2022).
- [57] J. Zhao, W. Wu, Y. Wang, and S. A. Yang, Electronic correlations in the normal state of the kagome superconductor KV_3Sb_5 , *Phys. Rev. B* **103**, L241117 (2021).
- [58] G. Blatter, M. V. Feigel'man, V. B. Geshkenbein, A. I. Larkin, and V. M. Vinokur, Vortices in high-temperature superconductors, *Rev. Mod. Phys.* **66**, 1125 (1994).
- [59] C. Buzea and T. Yamashita, Review of the superconducting properties of MgB_2 , *Supercond. Sci. Technol.* **14**, R115 (2001).
- [60] S. L. Li, H. H. Wen, Z. W. Zhao, Y. M. Ni, Z. A. Ren, G. C. Che, H. P. Yang, Z. Y. Liu, and Z. X. Zhao, Linear temperature dependence of lower critical field in MgB_2 , *Phys. Rev. B* **64**, 094522 (2001).
- [61] L. Shan, Y.-L. Wang, B. Shen, B. Zeng, Y. Huang, A. Li, D. Wang, H. Yang, C. Ren, Q.-H. Wang, S. H. Pan, and H.-H. Wen, Observation of ordered vortices with Andreev bound states in $Ba_{0.6}K_{0.4}Fe_2As_2$, *Nat. Phys.* **7**, 325 (2011).
- [62] A. Almoalem, A. Yagil, K. Cho, S. Teknowijoyo, M. A. Tanatar, R. Prozorov, Y. Liu, T. A. Lograsso, and O. M. Auslaender, Dependence of the absolute value of the penetration depth in $(Ba_{1-x}K_x)Fe_2As_2$ on doping, *Phys. Rev. B* **98**, 054516 (2018).
- [63] H. F. Hess, R. B. Robinson, R. C. Dynes, J. M. Valles, Jr., and J. V. Waszczak, Scanning-tunneling-microscope observation of the Abrikosov flux lattice and the density of states near and inside a fluxoid, *Phys. Rev. Lett.* **62**, 214 (1989).
- [64] W. Li, S. Pyon, A. Ichinose, S. Okayasu, and T. Tamegai, Suppression of superconductivity in heavy-ion irradiated $2H-NbSe_2$ caused by negative pressure, *J. Phys. Soc. Jpn.* **91**, 074709 (2022).